

Title: A Revision of the NASA Team Sea Ice Algorithm

Authors: T. Markus and D.J. Cavalieri

Submitted to: IEEE Transactions on Geoscience and Remote Sensing

Science Priorities:

Algorithm/Sensor Development

111 6/1
01 5 350

Abstract

In a recent paper, two operational algorithms to derive ice concentration from satellite multichannel passive microwave sensors have been compared. Although the results of these, known as the NASA Team algorithm and the Bootstrap algorithm, have been validated and are generally in good agreement, there are areas where the ice concentrations differ, by up to 30%. These differences can be explained by shortcomings in one or the other algorithm. Here, we present an algorithm which, in addition to the 19 and 37 GHz channels used by both the Bootstrap and NASA Team algorithms, makes use of the 85 GHz channels as well. Atmospheric effects particularly at 85 GHz are reduced by using a forward atmospheric radiative transfer model. Comparisons with the NASA Team and Bootstrap algorithm show that the individual shortcomings of these algorithms are not apparent in this new approach. The results further show better quantitative agreement with ice concentrations derived from NOAA AVHRR infrared data.

Title: A Revision of the NASA Team Sea Ice Algorithm

Authors: T. Markus and D.J. Cavalieri

Submitted to: IEEE Transactions on Geoscience and Remote Sensing

Significant Findings:

In this paper, we report the development a new algorithm to derive sea ice concentration from satellite passive microwave data. In contrast to commonly used algorithms, which use the 19 and 37 GHz channels, we obtain additional information by the use of the 85 GHz channels while correcting for their higher sensitivity to atmospheric effects by using an atmospheric radiative transfer model. Comparison with AVHRR imagery and National Ice center ice charts shows significant improvement over the results from current algorithms. Errors as large as 30% in these current algorithms are no longer apparent in the new results. This algorithm will be particularly useful for the EOS-PM AMSR mission.

A REVISION OF THE NASA TEAM SEA ICE ALGORITHM

Thorsten Markus

Code 971 NASA/GSFC-UMBC/JCET, Greenbelt, MD 20771, U.S.A.

Tel.: 301-614-5882, Fax: 301-614-5644, email: thorsten@beaufort.gsfc.nasa.gov

and

Donald J. Cavalieri

Code 971 NASA/GSFC, Greenbelt, MD 20771, U.S.A.

Submitted to IEEE Trans. Geoscience and Remote Sensing, March 1999.

1. Introduction

Accurate remote sensing of sea ice depends on knowing the emissivity of the ice, the physical temperature of the radiating portion of the ice, and the state of the atmosphere at the instant the ice is being observed. The difficulty is that these quantities are highly variable in space and time, particularly in the environment of the Arctic marginal seas and in the Southern Ocean. Sea ice emissivity depends on the physical, chemical and electrical properties of the ice, properties that are determined by the environmental conditions in existence during the growth phase of the ice as well as by the prevailing conditions when the ice is observed. Differences in salinity, ice thickness, snow cover, and surface wetness are only some of the factors that contribute to variations in microwave emission. The physical temperature of the radiating portion of the ice depends on the air temperature and the snow cover that insulates the ice from the atmosphere. In winter, air temperatures over the Antarctic pack ice, for example, range from 240 K to 270 K (see Fig. 2-7 in *Zwally et al.* [1983]), while snow conditions exhibit a variability from snow-free ice to ridged ice with a meter or more of snow [*Sturm et al.*, 1998].

Two widely used sea ice algorithms to derive sea ice concentrations from the DMSP SSM/I are the NASA Team (NT) algorithm [*Cavalieri et al.*, 1984; *Gloersen and Cavalieri*, 1986] and the Bootstrap (BS) algorithm [*Comiso*, 1995]. Difficulties with both these algorithms have been described by *Comiso et al.* [1997]. The comparative study revealed significantly different sea ice concentrations of up to 30% in some parts of the Antarctic with smaller although significant differences in parts of the Arctic. The study also identified potential reasons for the discrepancies including the influence of sea ice temperature variability on the BS retrievals and the influence of ice surface reflectivity variability on the emissivity at horizontal polarization in the NT retrievals. The latter problem effectively results in the existence of an additional radiometrically different ice type. The use of the low (19-37 GHz) SSM/I frequencies by these and other algorithms [*Steffen et al.*, 1992] limits the retrievals to resolving at most two ice types,

because of the high correlation of information content at these frequencies.

The challenge then was to find a combination of SSM/I channels that minimizes the effects of ice type and ice temperature variability while preserving a relatively large dynamic range to measure small changes in open water amount within the ice pack. We have taken the approach of revising the NT algorithm (the revised algorithm will be referred to as NT2), through the incorporation of the 85 GHz channels, while retaining both the relative insensitivity to ice temperature variations provided by radiance ratios and the relatively large dynamic range in sea ice concentration through the use of the 19 GHz channels. *Mätzler et al.* [1984] have shown that the sensitivity to inhomogeneities of the surface layer on the horizontal polarization at 85 GHz is much reduced and therefore have suggested the use of the 85 GHz channel for ice concentration retrievals if one can handle its higher sensitivity to atmospheric effects compared to the 19 GHz and 37 GHz channels. Others have investigated the use of the 85 GHz channels to derive ice concentrations at a higher spatial resolution. *Svendsen et al.* [1987] and *Lubin et al.* [1997] used the 85 GHz data with a simplified radiative transfer model. They obtained good results when cloud contamination was small [*Lubin et al.*, 1997]. Others used the 85 GHz data in successive combination with the low frequency channels to retrieve high resolution ice concentration [*St.Germain*, 1994], coastal polynya areas [*Markus and Burns*, 1995], or sea ice edges [*Hunewinkel et al.*, 1998] while correcting for atmospheric contributions in the 85 GHz data. Whereas *St.Germain* [1994] used a simplified radiative transfer model in order to make the radiative transfer equation invertible, here we handle this higher sensitivity to atmospheric effects through the use of forward calculations with a full atmospheric radiative transfer model [*Kummerow*, 1993] for various atmospheric scenarios which are used as a look-up table.

2. Description of the Algorithm

The two basic types of ratios of brightness temperatures, TB , used in the standard NT algorithm as well as in the NT2 approach are the polarization

$$PR(\nu) = \frac{TB(\nu V) - TB(\nu H)}{TB(\nu V) + TB(\nu H)} \quad (1)$$

and the spectral gradient ratio

$$GR(\nu_1 p \nu_2 p) = \frac{TB(\nu_1 p) - TB(\nu_2 p)}{TB(\nu_1 p) + TB(\nu_2 p)} \quad (2)$$

where ν is the frequency and p the polarized component (vertical or horizontal). Figure 1 shows a typical scatterplot of $PR(19)$ versus $GR(37V19V)$ for September conditions in the Weddell Sea. The NT algorithm identifies two ice types which are associated with first-year and multiyear ice in the Arctic and ice types A and B in the Antarctic (as shown in Figure 1). The AB-line represents 100% ice concentration. In this algorithm, the primary source of error is attributed to conditions in the surface layer such as surface glaze and layering [Comiso *et al.*, 1997], which can significantly affect the horizontally polarized 19 GHz brightness temperature [Mätzler *et al.*, 1984] leading to increased $PR(19)$ values and thus underestimates in ice concentration. In the following, we will call these surface effects. In Figure 1, pixels with significant surface effects create a cloud of points with lower ice concentrations (labeled C). For this reason, the BS algorithm uses primarily the 19 and 37 GHz vertically polarized channels and uses only selectively the 37 GHz horizontally polarized channel. While the NT algorithm uses radiance ratios to minimize ice physical temperature variability, the use of the SSM/I horizontally polarized channels makes it imperative to resolve a third ice type to overcome the difficulty of surface effects on the emissivity of the horizontally polarized component.

2.1. Approach

Because it has been shown that the horizontally polarized 85 GHz channel is much less affected by surface effects than the horizontally polarized 19 GHz channel [Mätzler *et al.*, 1984] and that 85 GHz based ice concentration retrievals can be satisfactorily obtained under clear conditions [e.g. Lubin *et al.*, 1998], our approach was to make use of the 85 GHz channels and find a way to reduce the associated atmospheric effects.

Starting from the NASA Team $PR(19) - GR(37V19V)$ domain (Figure 1), we rotate the axes by the angle between the GR -axis and the A-B line (FY-MY line for the Arctic), ϕ_{19} , to focus on the total ice concentration. This makes the A-B line vertical and the rotated PR , PR_R , is defined by

$$PR_R(19) = -GR(37V19V) \sin \phi_{19} + PR(19) \cos \phi_{19} \quad (3)$$

and is independent of ice types A and B. Calculation of total ice concentration using $PR_R(19)$ would be equivalent to the use of the NT algorithm. The angles expressed in radians are given in Table 1.

Next, because of the ambiguity of pixels with true low ice concentration and pixels with significant surface effects, we additionally make use of $GR(85V19V)$ and $GR(85H19H)$. These two ratios are highly correlated except for areas where surface effects decrease $TB(19H)$ and consequently increase $GR(85H19H)$ (Figure 2). Values of high $GR(85V19V)$ and high $GR(85H19H)$ are indicative of open water; the range of $GR(85H19H)$ values is larger because of the larger dynamic range between ice and water for the horizontally polarized components. With increasing ice concentration, the pixels move towards the diagonal. Pixels on the diagonal represent 100% ice concentration with different GR values corresponding to different ice types. When surface effects come into play, points deviate from this line towards increased $GR(85H19H)$ values while $GR(85V19V)$ remains constant (cloud of points to the right of the diagonal). This cloud of points corresponds to the cluster of points labeled C in Figure 1. Therefore the

difference between these two variables,

$$\Delta GR = GR(85H19H) - GR(85V19V), \quad (4)$$

will be used in the retrieval of ice concentration as an indicator of the presence of ice type C. Because of the higher sensitivity of the 85 GHz channels to atmospheric variability compared to the lower frequency channels, we need a third parameter to avoid the ambiguity between changes in ice concentration and changes in atmospheric conditions. Therefore, we calculate a $PR_R(85)$ from the $PR(85) - GR(37V19V)$ domain analogous to the calculation of $PR_R(19)$ with angles ϕ_{85} (Table 1). In Figure 3, ΔGR is plotted against $PR_R(19)$ (top) and $PR_R(85)$ (bottom) for the same region of the Weddell Sea as in Figure 1. Two primary clusters can be identified in each plot. One cluster with high PR and ΔGR values is representative of the open water with different atmospheric conditions causing primarily a reduction in the PR_R s. The other cluster with low PR_R and ΔGR values are pixels with high ice concentrations. The cloud of points in the NASA Team $PR - GR$ domain associated with surface effects (labeled C in Figure 1) has now become a linear cluster. Ice without surface effects has values close to zero in $PR_R(19)$ as well as in ΔGR . With increasing surface effects, $PR_R(19)$ increases and so does ΔGR . In agreement with the results from *Mätzler et al.* [1984], $PR_R(85)$ is nearly independent of surface effects resulting in an almost vertical cluster of points. Ice type C, which lies at the top end of the cluster and represents an ice type with a maximum amount of surface effects, is a radiometrically distinct ice type in this rotated domain. The scatter of points results partially from weather effects, partially from the natural variability in emissivity, and partially from real ice concentration changes. Because the data may be affected by varying atmospheric conditions, an atmospheric correction is necessary.

2.2. Atmospheric correction

In order to investigate quantitatively how different atmospheric conditions affect the data, we calculated brightness temperatures for the SSM/I channels using a forward atmospheric radiative transfer model [Kummerow, 1993] for the ice types and open water with different surface temperatures, different atmospheric temperature and humidity profiles, and different cloud conditions. The model considers absorption by water vapor and atmospheric oxygen as well as absorption and scattering by liquid and frozen hydrometeors. Model inputs are:

- Climatological winter and summer atmospheric temperature and humidity profiles from the Antarctic Georg-von-Neumayer station [König-Langlo, 1992].
- Surface emissivities from *Eppler et al.* [1992].
- Temperatures of the emitting surface:
 - Open water: 271 K
 - Sea ice, summer: 268 K
 - Sea ice, winter: 248 K
- Different cloud types from cirrus to cumulus congestus taken from *Fraser et al.* [1975] (Table 2).

Surface emissivities from *Eppler et al.* [1992] are adjusted to match the observed ratios such that under clear atmospheric conditions, the model ratios match the observed ratios.

The modeled $PR_R(19)$, $PR_R(85)$, and ΔGR values for different atmospheres over the three pure surface types are overlain in Figure 3 as gray circles. This shows that the model results in most cases span the width of the observed clusters. Clear atmosphere results have the lowest ΔGR and highest PR_R values for each surface type.

As shown by *Maslanik* [1992] for the Arctic and *Oelke* [1997] for the Antarctic, for 100% ice concentration weather effects result in significant changes in ice type in the NT algorithm but not in the total ice concentration. As a result of the rotation, $PR_R(19)$ is independent of changes in weather for ice covered areas and is reflected in the vertical orientation of the gray circles. In contrast to the $PR_R(19) - \Delta GR$ plot, the model shows a decrease in $PR_R(85)$ with increasing weather explaining the broader 100% ice concentration cluster.

Using the radiative transfer model, we calculate brightness temperatures for all the SSM/I channels and calculate $\langle PR_R(19) \rangle$, $\langle PR_R(85) \rangle$ and $\langle \Delta GR \rangle$ which are matrices containing all ice concentration combinations (0% to 100% in 1% increments) and the full range of atmospheric situations. Both the ice concentration and the atmospheric contribution are found by locating the the minimum of the quantity δR , defined by

$$\delta R = (PR_{Ri}(19) - \langle PR_R(19) \rangle)^2 + (PR_{Ri}(85) - \langle PR_R(85) \rangle)^2 + (\Delta GR_i - \langle \Delta GR \rangle)^2 \quad (5)$$

where $PR_{Ri}(19)$, $PR_{Ri}(85)$, and ΔGR_i are the ratios calculated from the observed brightness temperatures for a pixel i ; bracketed parameters indicate the modeled ratios.

3. Results

3.1. Hemispheric retrievals

Figures 4 and 5 show examples of winter time ice concentration retrievals for the northern and southern hemisphere, respectively, using the NT, the BS, and the NT2 algorithms. In the Arctic, all three algorithms give similar results except for the seasonal sea ice zones. As mentioned earlier, differences between the NT and BS algorithm are much larger in the Antarctic. One can clearly identify the areas of lower ice concentrations in the outer pack in the NT results (compared to the BS) which

result from the afore mentioned surface effects. On the other hand, the BS results reveal lower ice concentrations in the vicinity of the Antarctic continent resulting from the algorithm's sensitivity to physical temperature change. Neither of these deficiencies is apparent in the NT2 results. Detailed comparison with other data sets will be presented in section 4.

3.2. Reduction of weather effects

The effectiveness of the NT2 algorithm in reducing atmospheric effects both over the open ocean and in the marginal ice zone is illustrated by comparison with infrared data from the Optical Linescan System (OLS) onboard DMSP satellites. The appropriateness of the DMSP OLS is that it provides measurements spatially and temporally coincident with the SSM/I. Here, we use an overflight of the DMSP F-10 satellite in November 1992 over the Weddell Sea. Figure 6 shows an OLS image for November 12, 1992. Most cloud-covered regions can be identified by their bright swirly patterns. The corresponding SSM/I $PR(19)_R - \Delta GR$ and $PR(85)_R - \Delta GR$ scatterplots together with the model data are shown in Figure 7. Similar to Figure 3, the scatter of pixels for the pure surface types corresponds very well to the different modeled atmospheric scenarios. In Figure 8 (top row) the results from the NT and BS algorithms are presented for the same region shown in Figure 6. Using the new algorithm without the atmospheric model, the effect of weather is clearly visible over the open ocean (Figure 8, middle left). Using the atmospheric model (Figure 8, middle right) the cloud patterns over the ocean are greatly reduced. In the marginal ice zone, clouds lead to higher ice concentration without the weather correction but with the weather correction the distribution is smoother and ice concentration is reduced similar to the distribution of the BS algorithm. The difference map (Figure 8, bottom left) shows significant reductions in ice concentration for the open ocean and the marginal ice zone where clouds can be identified in the OLS image (Figure 6). The remaining erroneous

ice concentrations over the open ocean (<20%) may be the result of wind roughening and are easily eliminated using GR weather filters as used in the NT algorithm (Figure 8, bottom right).

Although these results suggest that the atmospheric contribution to the brightness temperatures at 85 GHz can be accounted for, very heavy cloud conditions can prevent the radiation emitted from the surface at 85 GHz from reaching the sensor. Analysis of both summer and winter season retrievals show that pixels exhibiting opaque conditions amount to less than 0.1%. For the open ocean, the NT GR weather filters are used so that extreme weather conditions are filtered beforehand.

3.3. Sensitivities to noise and atmospheric variations

In order to investigate how sensor noise propagates to the ice concentration estimates we vary the brightness temperatures for each SSM/I channel by ± 1 K, which corresponds to an upper limit of the sensor noise [Hollinger *et al.*, 1987]. This is done for three sets of brightness temperatures corresponding to ice concentrations of 32%, 51%, and 98%, respectively, in order to represent different ice cover scenarios. The results are presented in Table 3 and are approximately the same order of magnitude as for the NT algorithm [Swift and Cavalieri, 1985]. These noise sensitivity coefficients may also be used to estimate the effect of surface emissivity variations of the algorithm retrievals.

Next, it is necessary to understand how the limited set of atmospheres used in the algorithm may affect the results. Analogous to the study of sensor noise, we investigate three pixels with ice concentrations of 32%, 51%, and 98%. The variable δR from equation 5 provides a measure of the difference between the measured set of ratios and modeled ratios for each ice concentration combination and atmosphere. The values of δR are sorted by increasing difference. These, together with the corresponding ice concentrations are plotted in Figure 9. It shows that δR (top) reaches a distinct minimum and that the ice concentrations converge to an ice concentration of about

50% (bottom). In Figure 10, the smallest one hundred δR values together with the corresponding ice concentrations and atmospheric indices for the 32%, 51%, and 98% cases are presented. For the 32% and 51% cases δR is almost zero for the best solution meaning that there exists a set of modeled ratios which matches the measured ratios almost perfectly. For the 98% case the best δR is somewhat higher. For the 15 smallest differences, the ice concentrations vary only by $\pm 2\%$ for the 32% and 98% cases and by $\pm 1\%$ for the 51% case. Although the total ice concentrations are very stable for the last 15 solutions, oscillation in the atmospheric indices (Table 2) continues. For example, in the 32% case, oscillations occur between the atmospheric index 2 and 7, which represent a summer atmosphere with cirrus clouds (high water vapor, low cloud liquid water) and a winter atmosphere with more liquid water and less water vapor. Similar phenomena can be seen for the 51% and 98% cases. Other cases have been found where the atmosphere index oscillates between two odd or even values which correspond to the same season. This suggests that for those cases the “true” atmosphere has probably a liquid water content between the two modeled atmospheres. Because all of the SSM/I channels (except for the 22 GHz channel) lie in atmospheric “window” frequencies, the atmospheric contribution is generally rather small (even at 85 GHz). Therefore, we cannot retrieve atmospheric parameters over the highly emissive sea ice but we can reduce the “atmospheric noise” in the received radiances.

In Table 4, the ice concentrations with the best δR value separately for each atmosphere index (see Table 2) are listed. For the 32% case, the smallest δR corresponds to an atmosphere index of 7 followed by indices 2 and 4, which all have similar ice concentrations. The δR value is about an order of magnitude smaller for index 7 compared to indices 2 and 4. The range in ice concentration is approximately $\pm 10\%$ indicating the error range without atmospheric correction. The 51% case has about the same range. Here, δR is high for small atmosphere indices and has a distinct minimum at index 9 followed by index 6, which both give identical ice concentrations.

The range in ice concentrations is smaller for the 98% case ($\pm 5\%$) with smallest δR values for atmosphere with little liquid water content. This table demonstrates that the atmospheric correction is necessary and that finally retrieved ice concentration is stable; more in terms of total ice concentration than in terms of atmosphere index.

4. Comparisons with other data sets

The results of the NT2 algorithm are verified through a comparison with analyses from other data sources. For cloud-free conditions, this can be done with high resolution visible or infrared data from the NOAA AVHRR instrument. Because of the absence of solar illumination during the winter season only infrared data can be used during these periods.

For the comparison with infrared data, high resolution AVHRR LAC data have been gridded to a 1.5625 km SSM/I grid. A problem when using infrared data is that the regional variability of air and surface temperatures prohibits the calculation of AVHRR ice concentration using simple thresholds. Because of this problem, the mean and standard deviation of the AVHRR surface temperature for an area of consolidated ice are calculated for a 16×16 1.5625-pixel box (equivalent to 25×25 km). The minimum temperature plus 0.5 K (which is about the standard deviation in AVHRR surface temperature for consolidated ice) is taken to represent the 100% ice concentration temperature. The open water temperature is assumed to be 270 K. Ice concentrations are then calculated by a linear relationship between these two temperatures and the measured temperature.

4.1. Antarctic

A mostly cloud-free scene of the Ross Sea coincident with the maps shown in Figure 5 is presented in Figure 11. Except for a narrow coastal polynya along the Ross Ice Shelf and in Terra Nova Bay the sea ice is highly consolidated, although contains numerous

leads. A blow-up of the Ross Sea (Figure 12) shows that the NT algorithm seems to underestimate ice concentration in the outer pack and the BS algorithm seems to underestimate in the vicinity of the ice shelf (indicative of the deficiencies as discussed above and in *Comiso et al.* [1997]) whereas in the NT2 algorithm these deficiencies are not apparent. Analysis along a transect (black line in Figure 11) from the ice shelf towards the outer pack provides a more quantitative measure of the observed differences. In Figure 13a, we plot 270 minus the AVHRR channel 4 temperatures. The step function represents the derived ice temperatures for each 16×16 pixel box. After the coastal polynya adjacent to the shelf, the temperature decreases gradually until pixel 100. Leads can be identified as small peaks in the temperature curve. From about pixel 520 to pixel 550, some small polynyas have opened which are also recognizable in the image (Figure 11). The 25 km ice concentrations (Figure 13b) all capture the coastal polynya but only the NT2 algorithm shows a rapid increase in ice concentration in agreement with the AVHRR concentrations. Even small decreases in ice concentration are resolved with the new algorithm. In particular, the polynyas around pixel 33 are only noticeable in the NT2 results. This good agreement is also reflected in the correlation coefficient of 0.83 (compared to 0.65 for the NT and 0.50 for the BS algorithms (Table 5)). The small average difference of -0.8% (Table 5) shows that no significant bias is apparent. The better performance of the NT2 algorithm compared to the other two can be explained by the $PR(19)$, $GR(37V19V)$, and $PR(85)$ values (Figure 13c). Only at $PR(85)$ do the two polynya areas result in distinct peaks. From pixel 5 to pixel 20, $PR(19)$ is fairly constant, whereas $GR(37V19V)$ decreases from 0.0 to -0.03 . This indicates a probable increase in snow cover, so that by pixel 20 the snow cover is sufficient to insulate the snow-ice interface from the surface, and the BS algorithm reaches 100% ice concentration. Also, at this point the NT ice concentrations begin to decrease as a result of an increase in $PR(19)$. Because $GR(37V19V)$ stays at values well below zero, this increase in $PR(19)$ is probably caused by surface effects. This increase is not seen

in $PR(85)$.

4.2. Arctic

Figure 14 shows a portion of the Greenland Sea from Figure 4. In general, the three algorithms give similar results, but there are significant local differences. At the southern part of the Odden sea ice tongue, the ice concentrations are higher in the NT2 results (70% to 80%) compared to the NT and the BS results (60% to 70%). North of this area there is a band of ice concentrations between 50% and 60% in the NT2 results (40% to 50% in the NT and BS results). In Figure 15, an ice concentration chart from the National Ice Center is presented. As one can see from the legend, the ice concentrations are derived from visible/infrared and radar images giving an estimate not dependent on SSM/I data. This chart shows that the ice concentrations from the NT2 algorithm are in better agreement with the NIC ice chart than the NT and the BS ice concentrations are.

In Figure 16, a cloud-free AVHRR scene for the Sea of Okhotsk during February 4, 1995 is presented. The corresponding SSM/I-derived ice concentrations are presented in Figure 17. Overall, the three ice concentration algorithms give similar results. A transect was chosen (black line in Figure 16) and the ice concentrations derived (Figure 18) as was done for the Antarctic. Because the AVHRR surface temperatures are much more variable than in the Antarctic transect, the standard deviation for consolidated ice was 3 K which was again added to the minimum temperature for each 16×16 pixel box and assumed to be representative of the 100% ice concentration temperature (Figure 18a). All of the algorithms resolve the open water at pixel 7 (Figure 18b). For this transect, the correlation coefficients are more comparable (Table 6). Nevertheless, the NT2 algorithm has the highest correlation coefficient and the smallest bias.

5. Conclusion

In this paper, we present a new algorithm to derive ice concentrations from satellite passive microwave data. While continuing to use ratios in order to make a first-order correction for changes in physical temperature as in the NT algorithm, we also use data from the 85 GHz channels together with an atmospheric radiative transfer model to correct for weather effects particularly in the 85 GHz data. The results have shown that the algorithm gives better agreement with AVHRR data for both hemispheres and that the suspected deficiencies in the NT and BS algorithms are not present with this new approach.

For the future, we are planning to make better use of the high resolution information provided by the 85 GHz channels. This is of particular importance for the upcoming AMSR instrument where the 89 GHz channels have a sampling rate of 5 km and a spatial resolution of 4 km x 6 km. Additionally, we will explore different approaches to match ice concentration results from these sensors (e.g. SSM/I and AMSR) with those from the SMMR (where no 85 GHz data were available) in order to continue in the long continuous time series of ice concentrations beginning 1978.

Acknowledgments

We thank NSIDC for the SSM/I brightness temperature data distributed on CD-ROM and the NOAA Satellite Active Archive for the AVHRR data. This work was supported by the NASA EOS-PM project.

References

- Cavalieri, D. J., A microwave technique for mapping thin sea ice, *J. Geophys. Res.*, *99*, 12,561-12,572, 1994.
- Cavalieri, D.J., P. Gloersen, and W.J. Campbell, Determination of sea ice parameters with the NIMBUS 7 scanning multichannel microwave radiometer, *J. Geophys. Res.*, *89*, 5355-5369, 1984.
- Comiso, J.C., SSM/I sea ice concentrations using the bootstrap algorithm, *NASA Reference Publication*, *1380*, 49 pp., 1995.
- Comiso, J. C., D. J. Cavalieri, C. L. Parkinson, and P. Gloersen, Passive microwave algorithms for sea ice concentration - A comparison of two techniques, *Remote Sens. Environ.*, *60*, 357-384, 1997.
- Eppler, D.T., and 14 others, Passive microwave signatures of sea ice, in *Microwave Remote Sensing of Ice*, *Geophys. Monogr. Ser.*, vol. 68, edited by F. Carsey, pp. 47-71, AGU, Washington, D.C., 1992.
- Fraser R.S., Gaut, N.E., Reifenstein, E.C., and H. Sievering, Interaction Mechanisms—Within the Atmosphere, in *Manual of Remote Sensing*, edited by R.G. Reeves, A. Anson, D. Landen, pp.181-233, American Society of Photogrammetry, Falls Church, VA, 1975.
- Gloersen, P. and D.J. Cavalieri, Reduction of weather effects in the calculation of sea ice concentration from microwave radiances, *J. Geophys. Res.**91*, 3913-3919, 1986.
- Hollinger, J., R. Lo, G. Poe, R. Savage, and J. Pierce, Special Sensor Microwave/Imager User's Guide, *Naval Research Laboratory*, 1987.
- Hunewinkel, T., T. Markus, and G.C. Heygster, Improved determination of the sea ice edge with SSM/I data for small-scale analyses, *IEEE Trans. Geosc. Rem. Sens.*, *36*, 1795-1808, 1998.
- König-Langlo, G., The meteorological data of the Georg-von-Neumayer-Station (Antarctica) for 1988, 1990, 1991, *Rep. Polar Research*, *116*, 70 pp., Alfred-

- Wegener-Institut für Polar- und Meeresforschung, Bremerhaven, Germany, 1992.
- Kummerow, C., On the accuracy of the Eddington approximation for radiative transfer in the microwave frequencies, *J. Geophys. Res.*, *98*, 2757-2765, 1993.
- Lubin, D., C. Garrity, R.O. Ramseier, and R.H. Whritner, Total sea ice concentration retrieval from the SSM/I 85.5 GHz channels during the Arctic summer, *Rem. Sens. Environ.*, *62*, 63-76, 1997.
- Markus, T. and B.A. Burns, A method to estimate sub-pixel scale coastal polynyas with satellite passive microwave data, *J. Geophys. Res.*, *100*, 4473-4487, 1995.
- Maslanik, J.A., Effects of weather on the retrieval of sea ice concentration and ice type from passive microwave data, *Int. J. Rem. Sens.*, *13*, 34-57, 1992.
- Mätzler, C., R.O. Ramseier, and E. Svendsen, Polarization effects in sea-ice signatures, *IEEE J. Oceanic Eng.*, *OE-9*, 333-338, 1984.
- Oelke, C., Atmospheric signatures in sea-ice concentration estimates from passive microwave: modeled and observed, *Int. J. Remote Sensing*, *18*, 1113-136, 1997.
- St. Germain, K.M., A two-phase algorithm to correct for atmospheric effects on the 85 GHz channels of the SSM/I in the Arctic region, *Proceedings IGARSS'94*, 148-151, 1994.
- Steffen, K., J. Key, D.J. Cavalieri, J.C. Comiso, P. Gloersen, K. St.Germain, and I. Rubinstein, The estimation of geophysical parameters using passive microwave algorithms, in *Microwave Remote Sensing of Ice, Geophys. Monogr. Ser.*, vol. 68, edited by F. Carsey, pp. 201-231, AGU, Washington, D.C., 1992.
- Sturm, M., K. Morris, and R. Massom, The character and distribution of the winter snow cover on the sea ice of the Bellingshausen, Amundsen, and Ross Seas, Antarctica, 1994-1995, in *Antarctic Sea Ice: Physical Processes, Interactions, and Variability, Antarctic Research Series*, *74*, edited by M.O. Jeffries, pp.1-18, AGU, Washington, D.C., 1998.

Svendsen, E., C. Mätzler, and T.C. Grenfell, A model for retrieving total sea ice concentration from a spaceborne dual-polarized passive microwave instrument operating at 90 GHz, *Int. J. Remote Sensing*, 8, 1479-1487, 1987.

Swift, C.T. and D.J. Cavalieri, Passive microwave remote sensing of sea ice research, *EOS*, 66, 1210-1212, 1985.

Zwally H. J., J. C. Comiso, C. L. Parkinson, W. J. Campbell, F. D. Carsey, P. Gloersen, Antarctic sea ice, 1973-1976: Satellite passive-microwave observations, *NASA SP-459*, 206 pp., 1983.

Table 1. Angles in radians between the GR -axis and the A-B line (FY-MY line for the Arctic) for the $PR(19) - GR(37V19V)$ domain and the $PR(85) - GR(37V19V)$ domain.

Hemisphere	ϕ_{19}	ϕ_{85}
Antarctic	-0.59	-0.40
Arctic	-0.18	-0.06

Table 2. Model atmospheres.

#	Season	Cloud type	LWC [g m^{-2}]	Base height [km]	Top height [km]
0	summer	clear	0.0	n/a	n/a
1	winter	clear	0.0	n/a	n/a
2	summer	cirrus	50.0	5.0	5.5
3	winter	cirrus	50.0	5.0	5.5
4	summer	stratus	15.0	0.4	0.7
5	winter	stratus	15.0	0.4	0.7
6	summer	stratus cumulus	75.0	0.5	1.0
7	winter	stratus cumulus	75.0	0.5	1.0
8	summer	stratus cumulus	125.0	0.5	1.0
9	winter	stratus cumulus	125.0	0.5	1.0
10	summer	cumulus congestus	250.0	1.0	3.0
11	winter	cumulus congestus	250.0	1.0	3.0

Table 3. Calculated ice concentrations resulting from changes in brightness temperatures by ± 1 K for each channel. The bottom row is the RMS change for all channels i .

Δ K	C=32%		C=51%		C=98%	
	+1 K	-1 K	+1 K	-1 K	+1 K	-1 K
19V	34	31	52	49	99	95
19H	32	32	51	51	98	98
37V	31	33	50	52	95	99
85V	30	34	49	53	94	100
85H	34	30	45	48	100	94
$\sqrt{\sum_i (\Delta C_i)^2}$	3.6	3.2	6.5	4.2	5.3	5.5

Table 4. Ice concentrations with the smallest δR for each atmosphere separately for the 32%, 51%, and 98% cases.

Atm. Idx	C=32%		C=51%		C=98%	
	IC	δR	IC	δR	IC	δR
0	40	2.5E-5	61	7.0E-5	96	1.4E-6
1	44	1.2E-4	64	1.7E-4	98	1.3E-6
2	34	1.6E-6	58	1.2E-5	93	3.9E-6
3	39	6.6E-5	61	1.2E-4	96	2.0E-6
4	37	3.0E-6	60	1.5E-5	94	2.3E-6
5	42	3.4E-5	63	8.0E-5	97	2.3E-6
6	29	6.1E-5	51	1.6E-6	94	5.5E-5
7	32	1.8E-7	59	3.3E-6	94	1.5E-5
8	28	4.1E-4	44	9.7E-6	94	1.6E-4
9	29	8.4E-5	51	3.2E-7	94	7.8E-5
10	23	1.4E-3	40	3.1E-4	94	4.1E-4
11	23	8.9E-4	41	1.3E-4	94	3.0E-4

Table 5. Correlation coefficient between the ice concentrations from AVHRR and the three SSM/I algorithms for the Ross Sea transect as plotted in Figure 13b as well as the average difference.

Algo.	Corr.Coeff.	$\overline{C_{AVHRR} - C_{SSM/I}}$
NT	0.65	7.9
BS	0.50	2.2
NT2	0.83	-0.8

Table 6. Correlation coefficient between the ice concentrations from AVHRR and the three SSM/I algorithms for the Sea of Okhotsk transect as plotted in Figure 18b as well as the average difference.

Algo.	Corr.Coeff.	$\overline{C_{AVHRR} - C_{SSM/I}}$
NT	0.71	1.6
BS	0.65	-7.2
NT2	0.74	-1.1

Figure 1. $GR(37V19V)$ versus $PR(19)$ for September 15, 1992 in the Weddell Sea. The gray circles represent the tiepoints for the ice types A and B as well as for open water as used by the NT algorithm. The circled area, labeled C, indicates pixels with significant surface effects.

Figure 2. $GR(85H19H)$ versus $GR(85V19V)$ for the same data set as in Figure 1.

Figure 3. ΔGR versus $PR_R(19)$ (top) and ΔGR versus $PR_R(85)$ (bottom) for the same data set as in Figure 1. The gray circles represent the modeled ratios for the three pure surface types with different atmospheric conditions.

Figure 4. Ice concentration retrievals for the Arctic, January 27, 1997 using the three different algorithms.

Figure 5. Ice concentration retrievals for the Antarctic, August 23, 1993 using the three different algorithms.

Figure 6. DMSP OLS infrared data for an overflight at September 12, 1992.

Figure 7. ΔGR versus $PR_R(19)$ (top) and ΔGR versus $PR_R(85)$ (bottom) for the single swath data presented in Figure 8. The gray circles represent the modeled ratios for the three pure surface types with different atmospheric conditions.

Figure 8. SSM/I derived ice concentrations from a DMSP F-10 overflight for September 12, 1992. Top row: Ice concentration using the NT and BS algorithms. Middle row: Ice concentration using the NT2 algorithm without atmospheric correction (left) and with atmospheric correction (right). Bottom row: Difference between the NT2-derived ice concentration without and with atmospheric correction (left) (white pixels indicate negative differences of about 1%); final NT2 ice concentration using the NT GR weather filter (right).

Figure 9. All of the possible 60000 δR values (sorted by increasing δR value) and the corresponding ice concentration for a finally retrieved ice concentration of 51%.

Figure 10. Smallest 100 δR s with corresponding ice concentrations and atmospheric indices for the 32% case (left column), the 51% case (middle column), and the 98% case (right column).

Figure 11. AVHRR infrared data for the Ross Sea coincident with the data in Figure 5.

Figure 12. Subset of Figure 5 for the Ross Sea.

Figure 13. Transect through the Ross Sea (black line in Figure 11). AVHRR infrared data and reference 100% ice concentration temperatures derived from 16×16 pixels boxes (a); ice concentrations derived from the SSM/I data using the NT, BS, and NT2 algorithms as well as derived from the AVHRR temperatures (b); brightness temperature ratios (c).

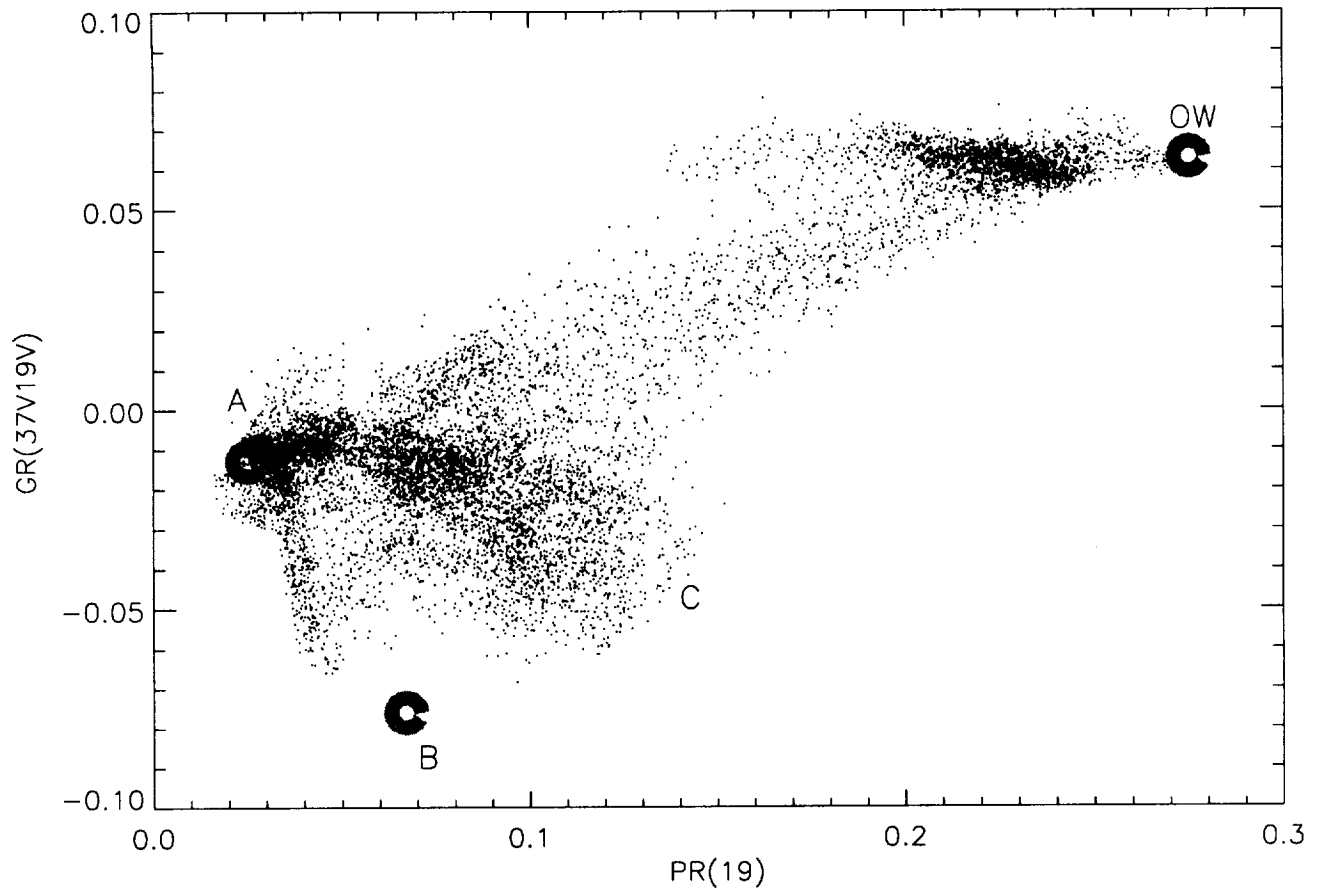
Figure 14. Subset of Figure 4 for the Greenland Sea.

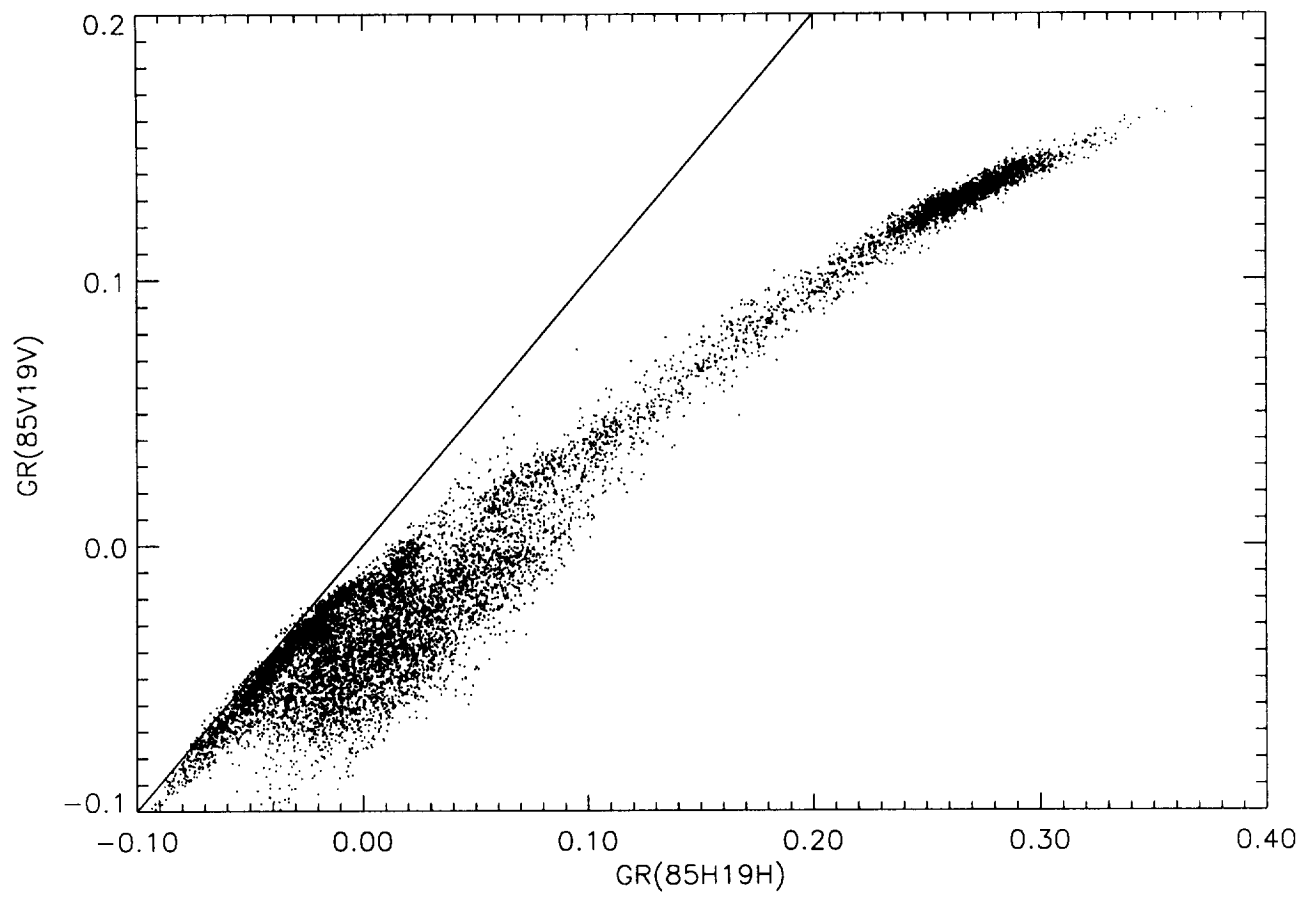
Figure 15. Ice chart from the National Ice Center coincident with the data in Figure 4. The total ice concentrations (or range of) for each polygon are indicated in the uppermost group of the ice chart symbology, expressed in tenths.

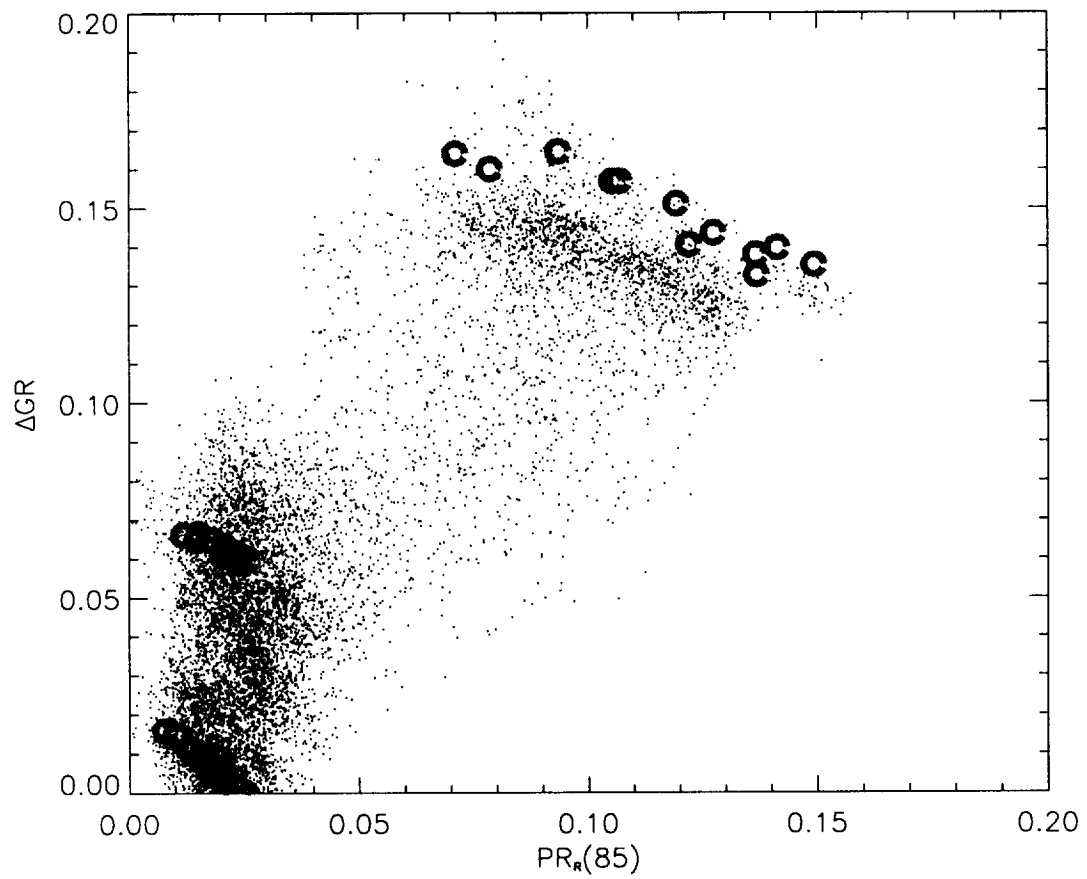
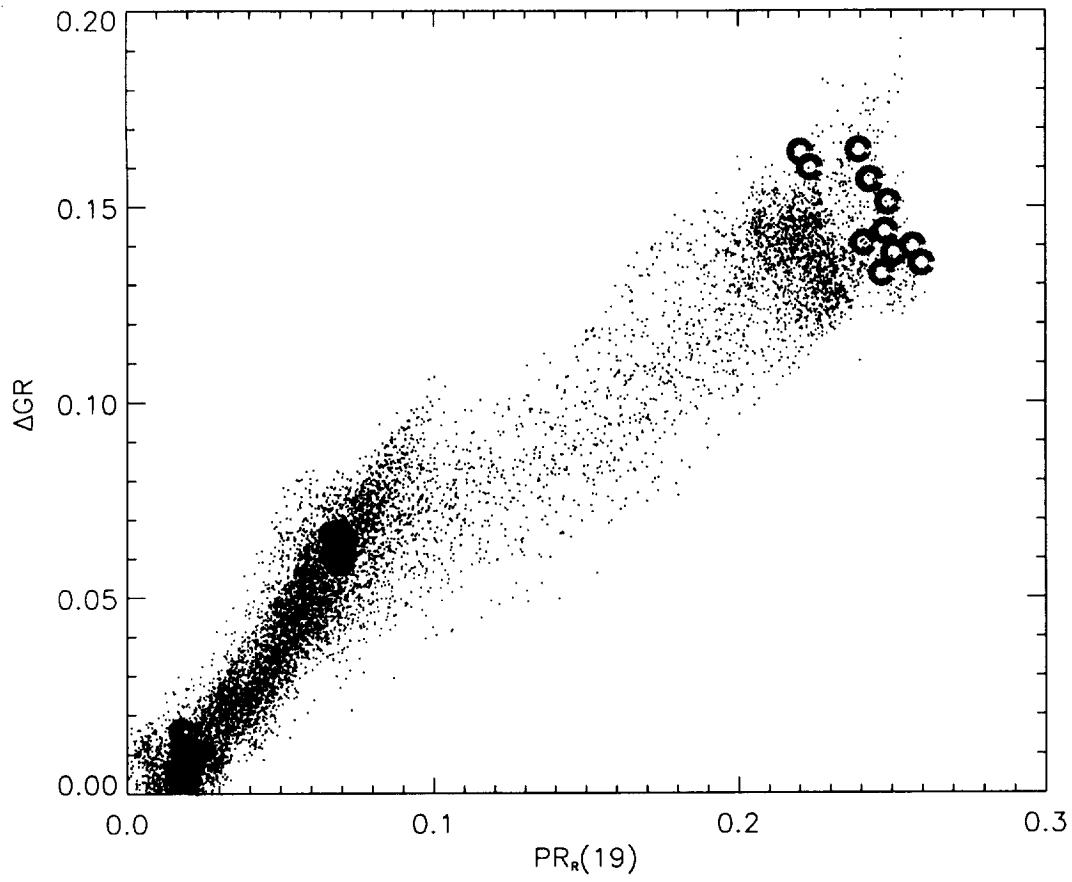
Figure 16. AVHRR infrared data for the Sea of Okhotsk for February 4, 1995.

Figure 17. SSM/I derived ice concentration for the Sea of Okhotsk during February 4, 1995.

Figure 18. Transect through the Sea of Okhotsk (black line in Figure 16). AVHRR infrared data and reference 100% ice concentration temperatures derived from 16×16 pixels boxes (a); ice concentrations derived from the SSM/I data using the NT, BS, and NT2 algorithms as well as derived from the AVHRR temperatures (b); brightness temperature ratios (c).





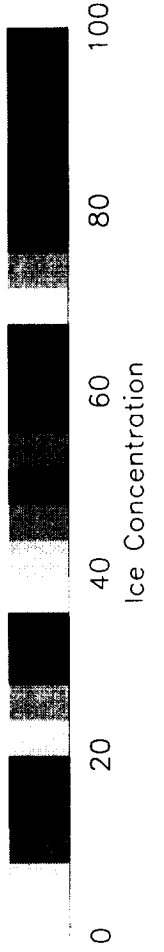
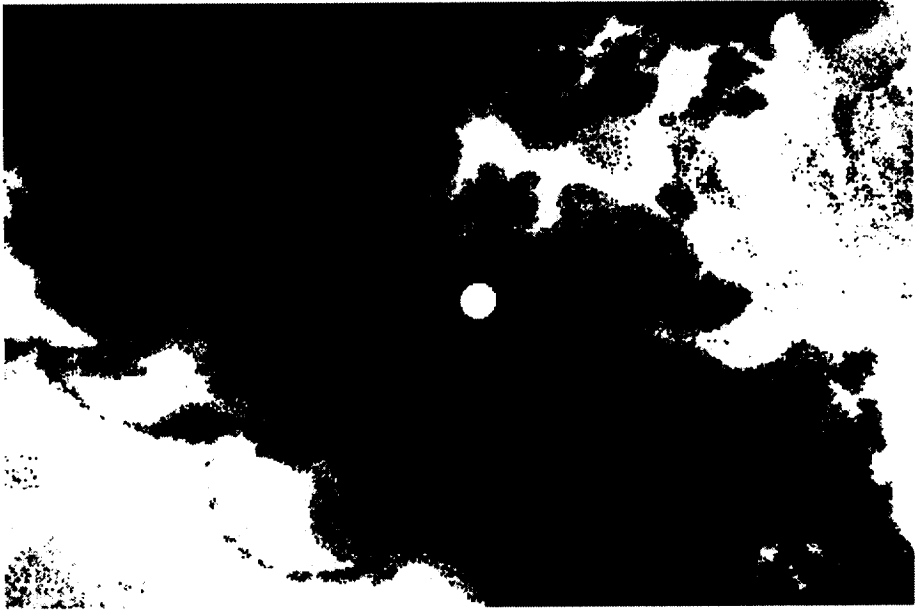


Ice Concentrations January 27, 1997

NASA Team

Bootstrap

NT2

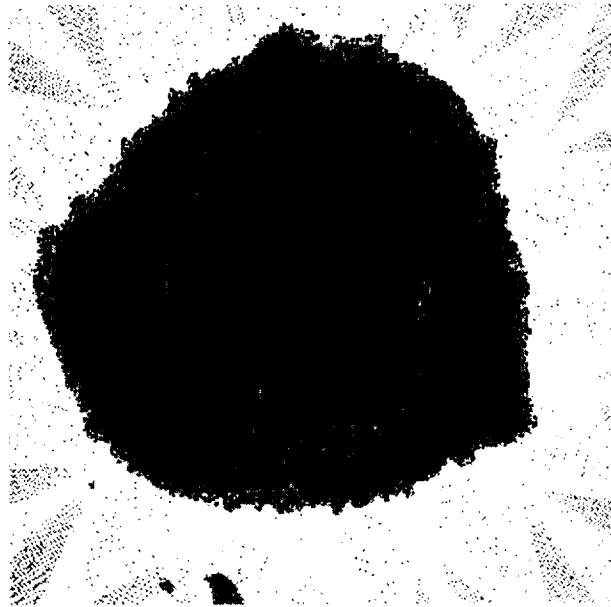


Ice Concentrations September 30, 1992

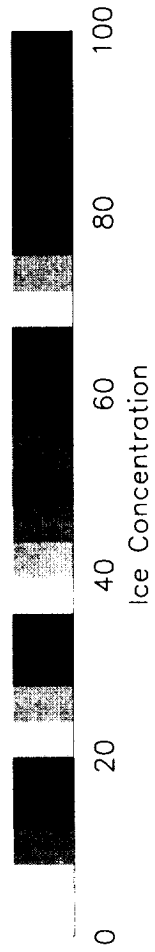
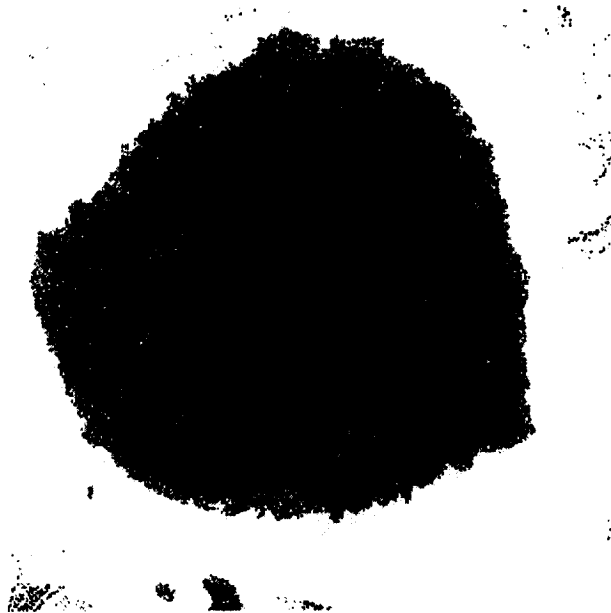
Nasa Team



Bootstrap



NT 2





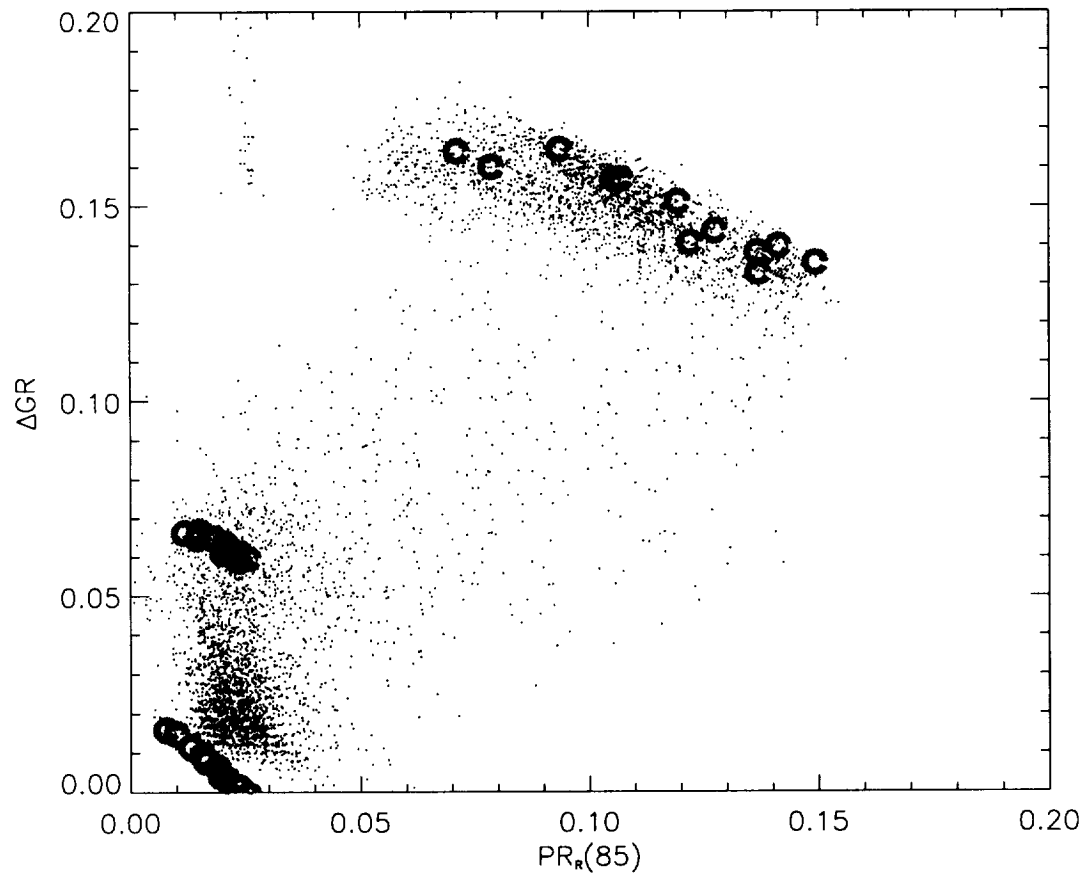
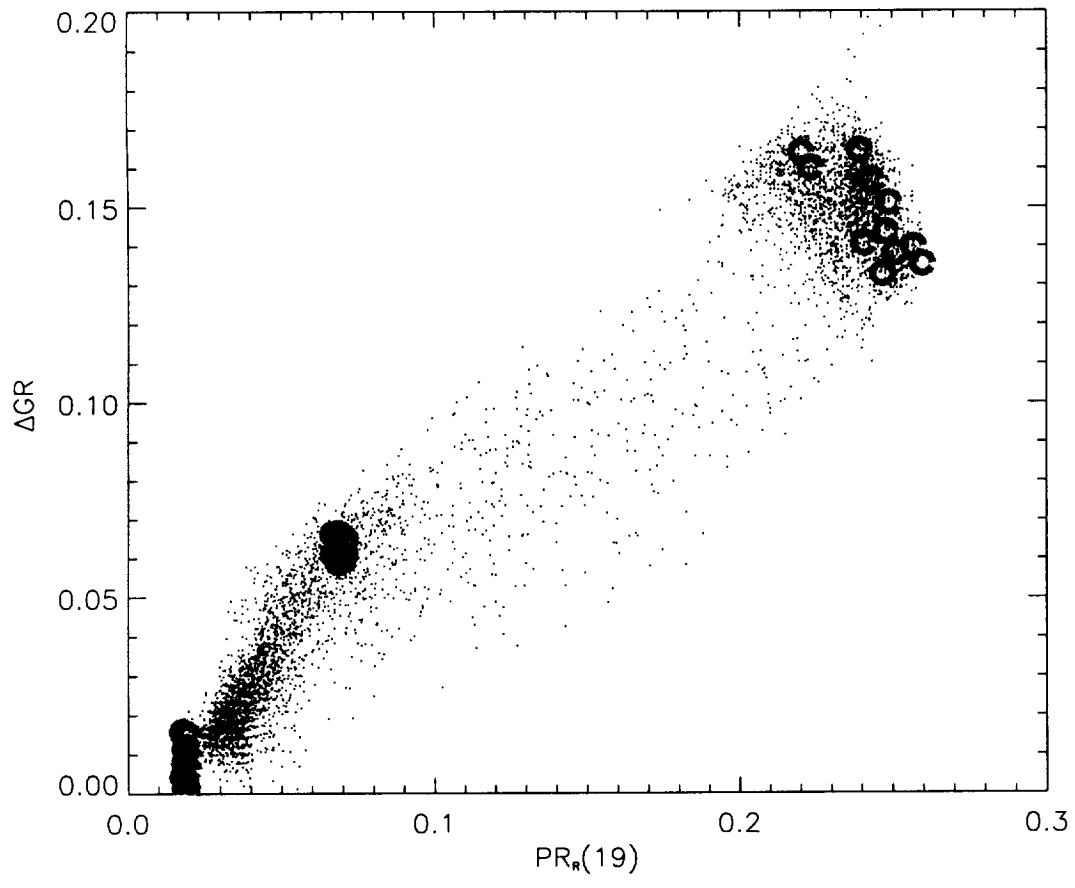


Fig. 7

NASA Team

Bootstrap



NT2 without Wx corr

NT2 with Wx corr



NT2 w/o Wx corr - NT2 w/ Wx corr

NT2 with Wx corr and GR Wx filter

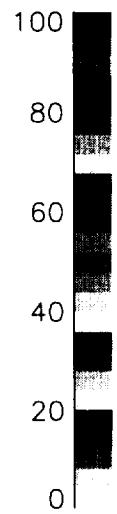
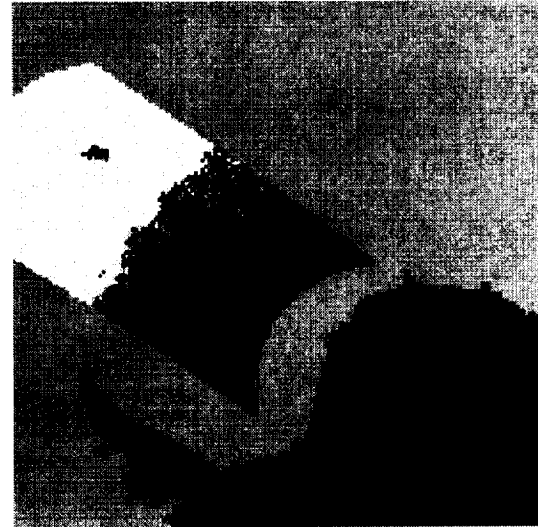


Fig. 8

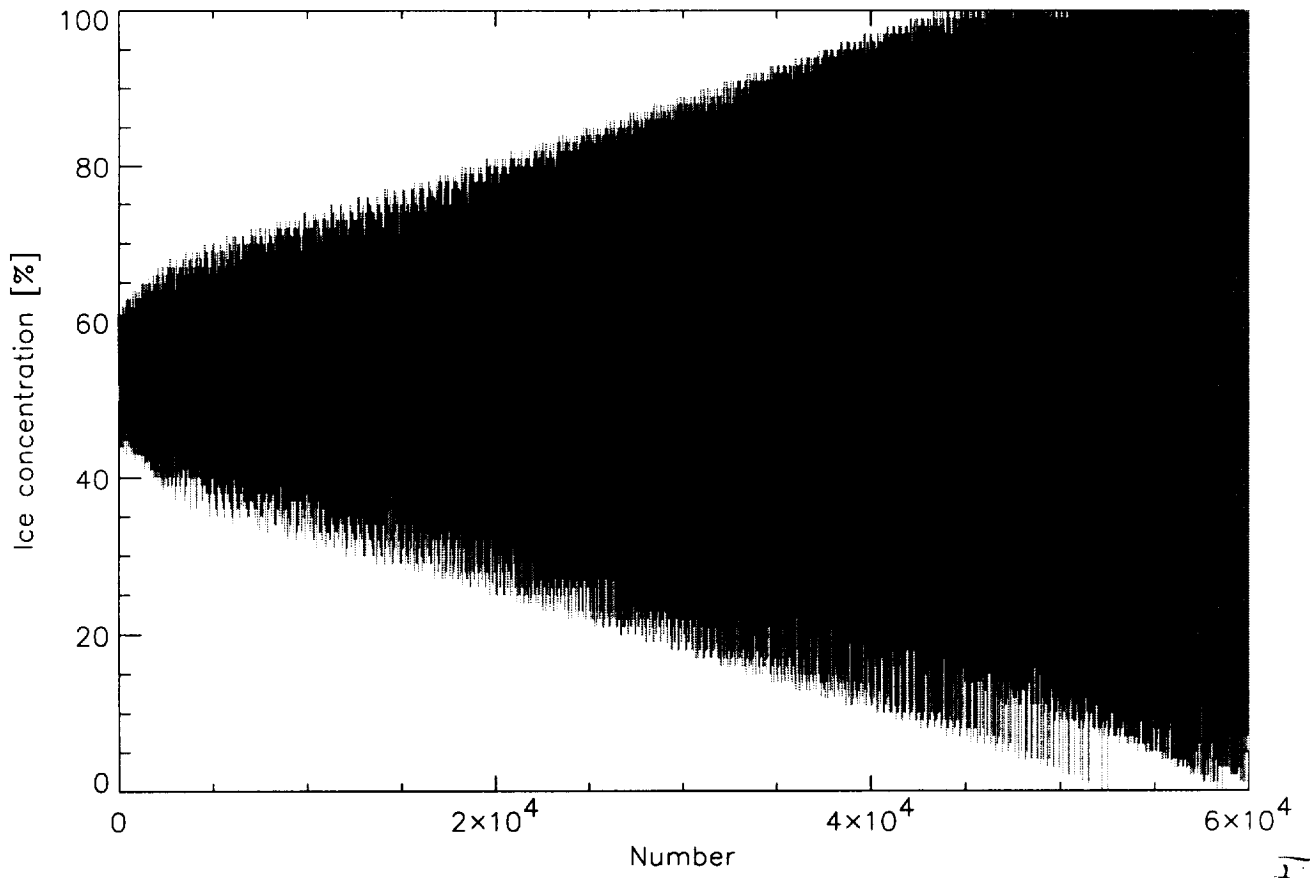
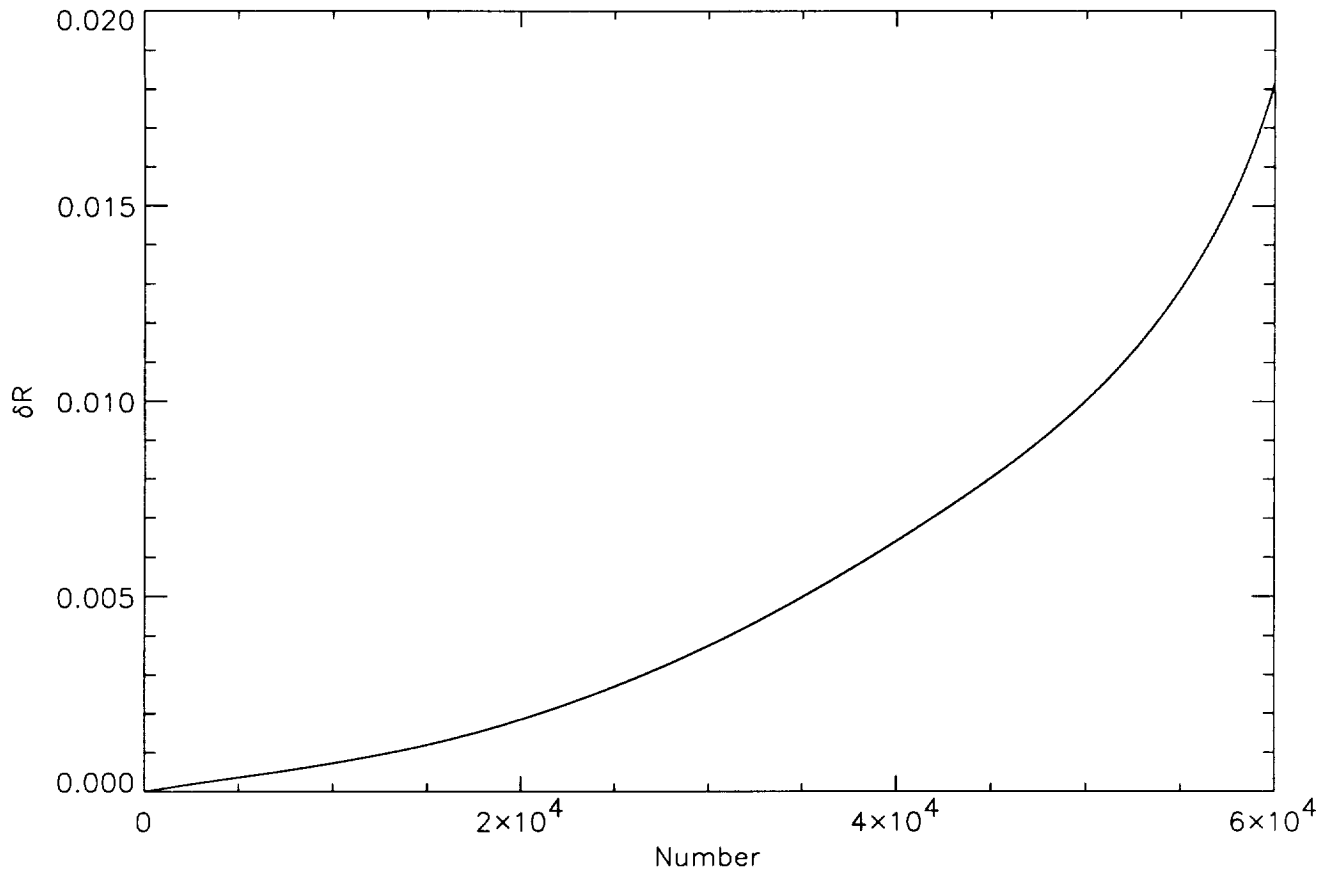


Fig. 9

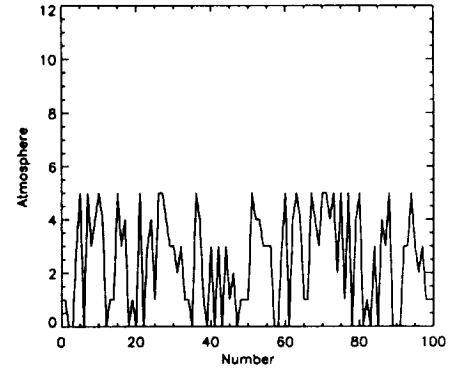
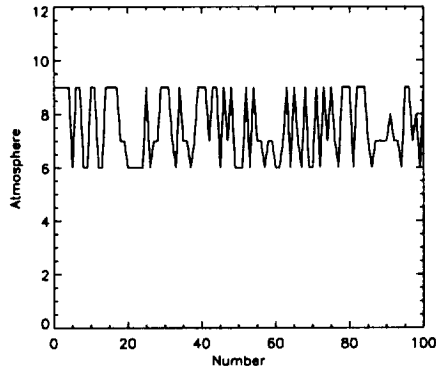
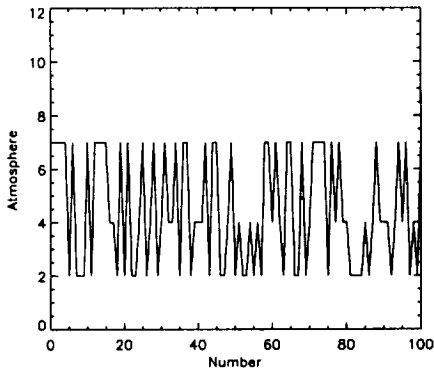
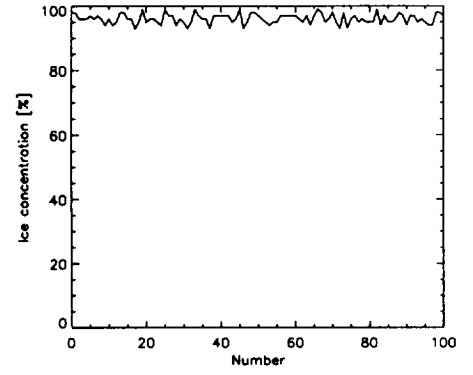
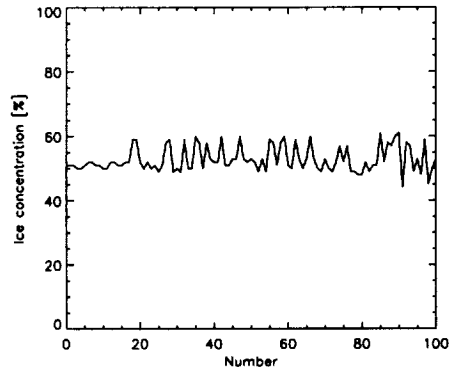
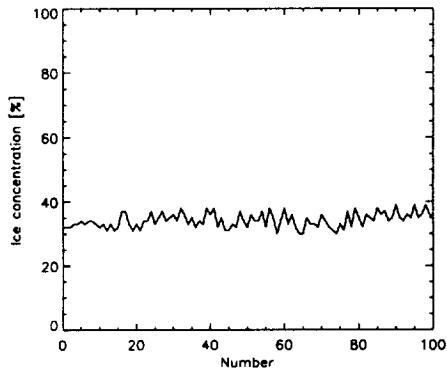
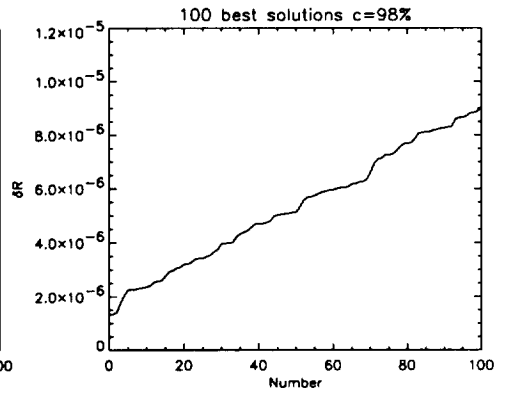
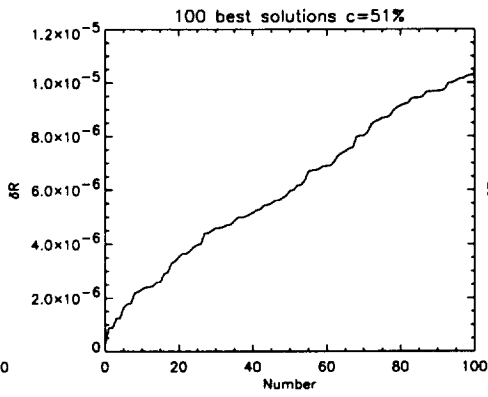
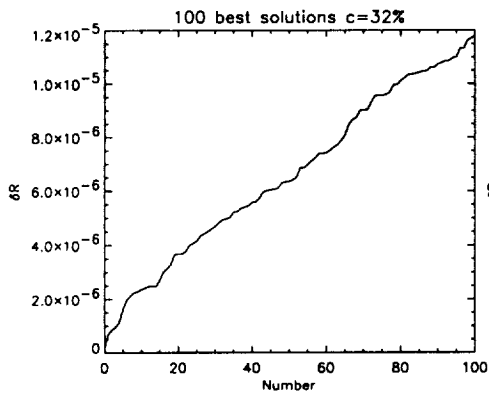
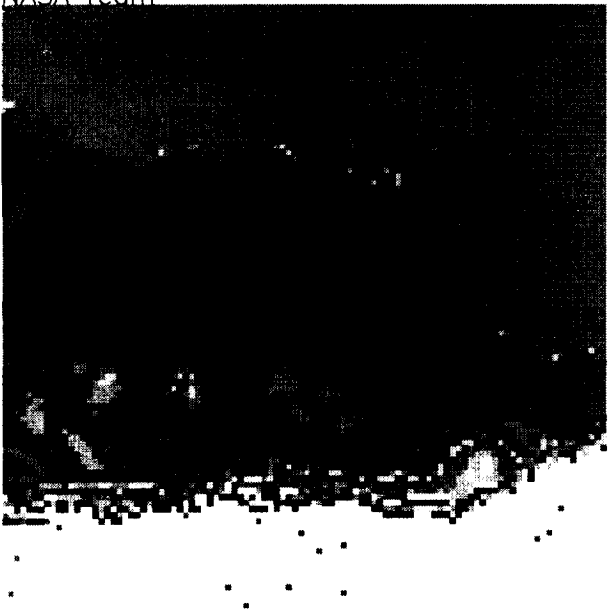


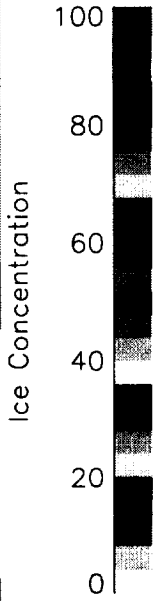


Fig. 11

NASA Team

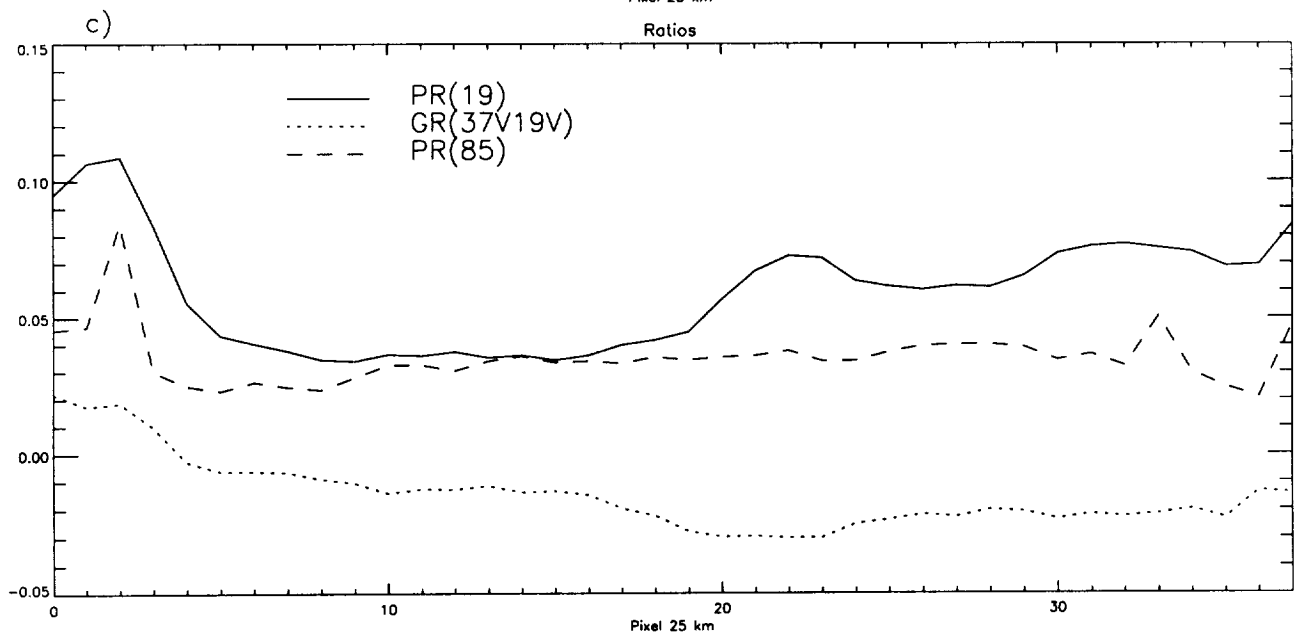
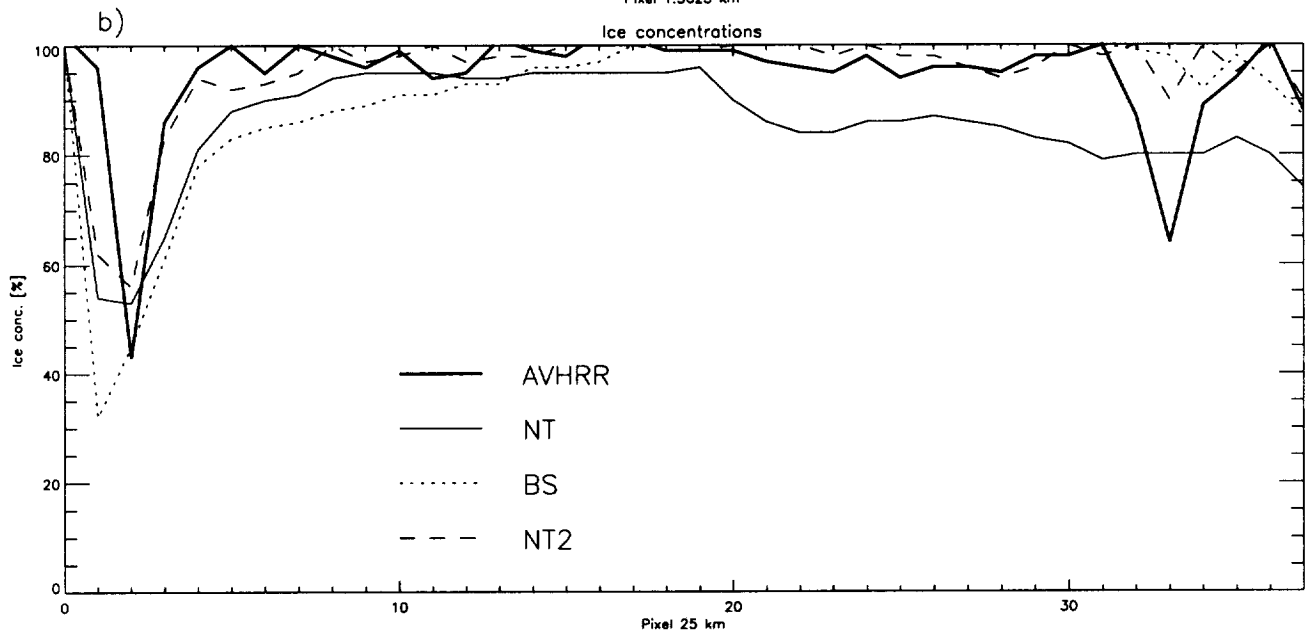
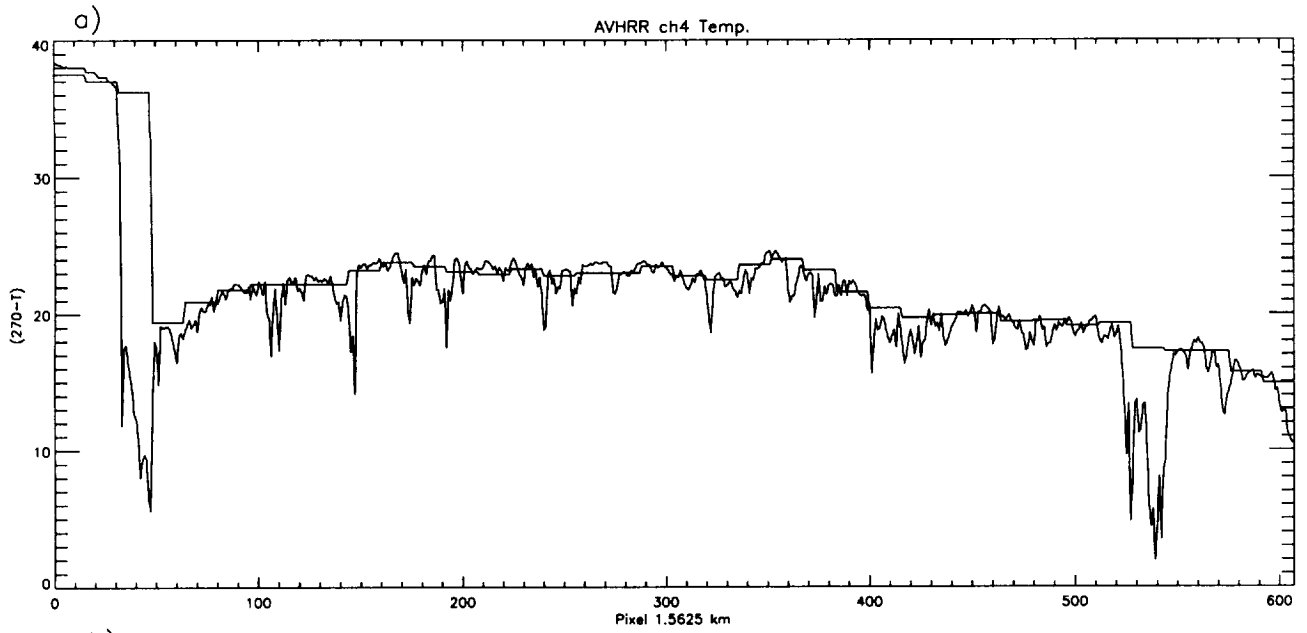


Bootstrap

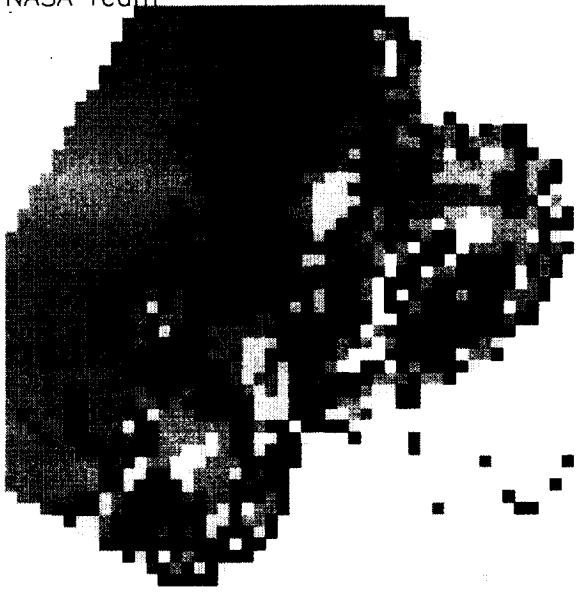


NT2

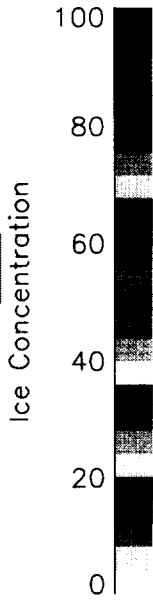
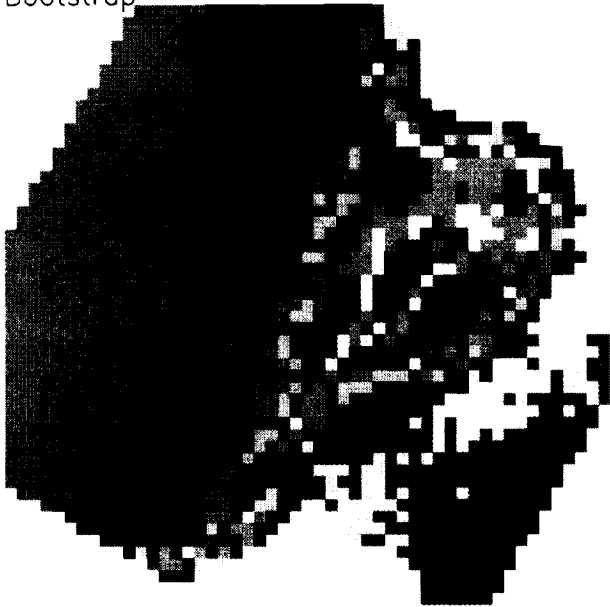




NASA Team



Bootstrap



NT2

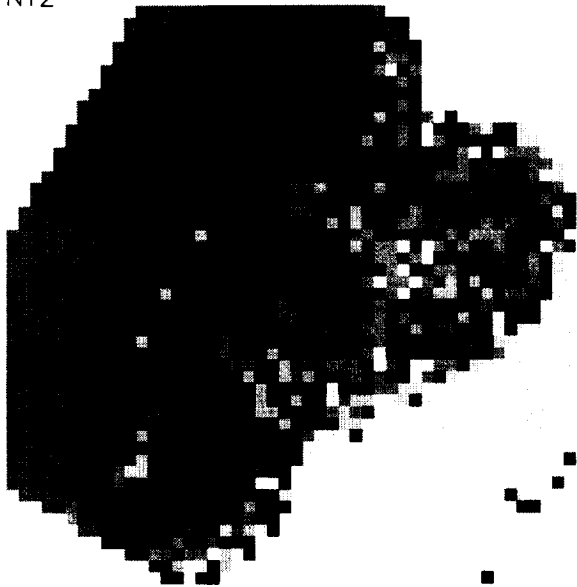
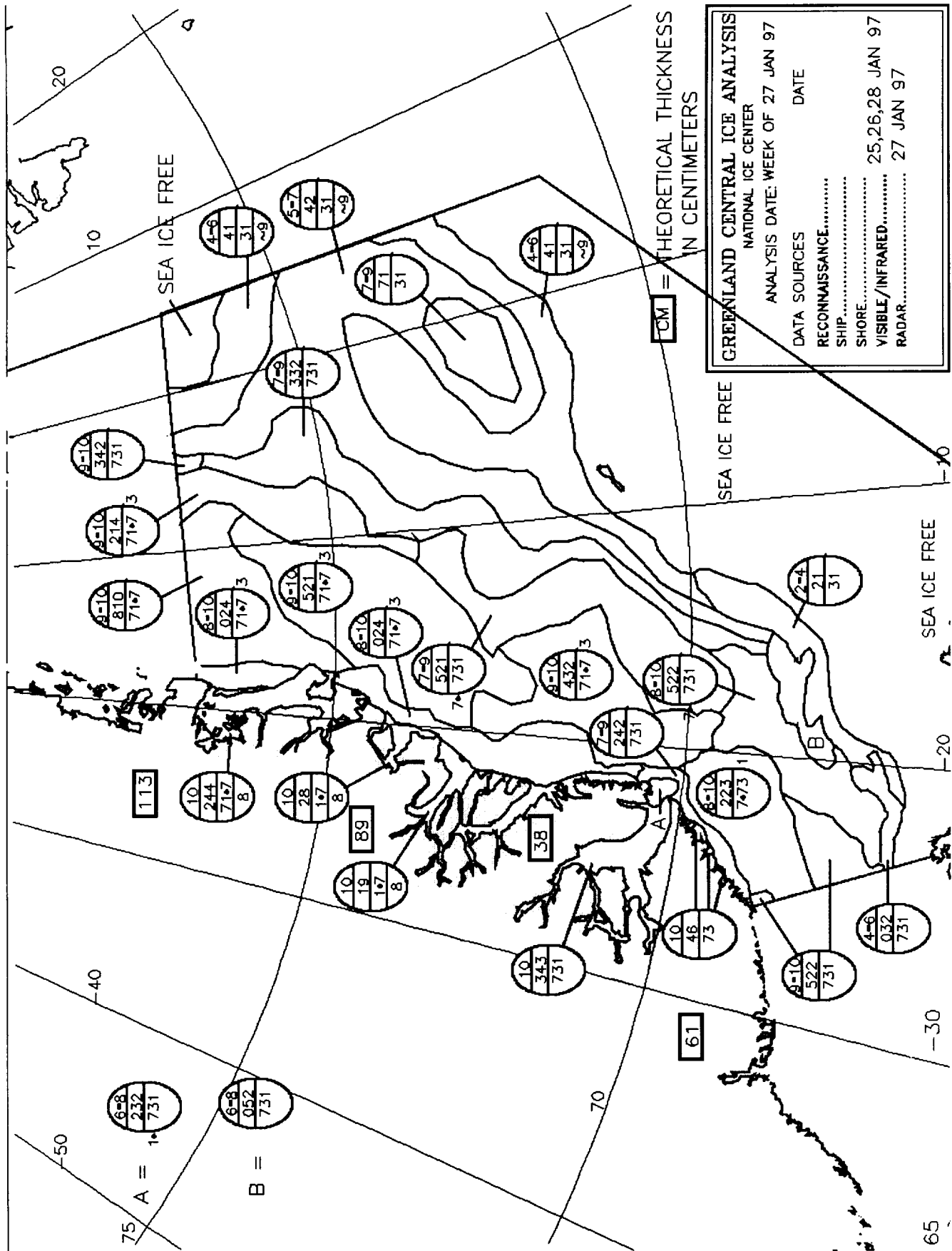


Fig. 14



GREENLAND CENTRAL ICE ANALYSIS
 NATIONAL ICE CENTER
 ANALYSIS DATE: WEEK OF 27 JAN 97
 DATA SOURCES
 RECONNAISSANCE.....
 SHIP.....
 SHORE..... 25,26,28 JAN 97
 VISIBLE/INFRARED.....
 RADAR..... 27 JAN 97

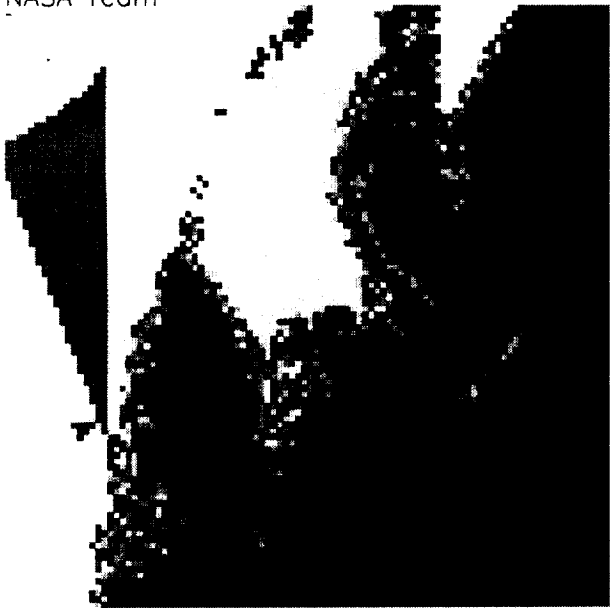
75 A = 1
 B =

15-15

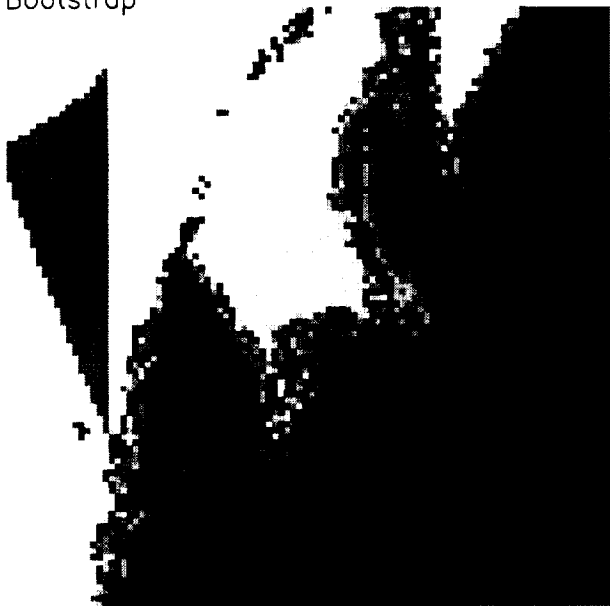


Fig. 16

NASA Team



Bootstrap



NT2

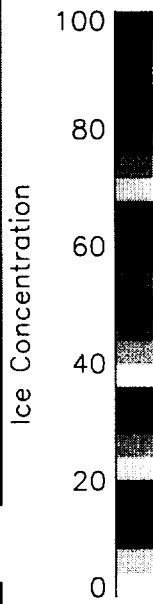


Fig. 17

